Article

$CoMnO_2$-Decorated Polyimide-Based Carbon Fiber Electrodes for Wire-Type Asymmetric Supercapacitor Applications

Young-Hun Cho [1], Jae-Gyoung Seong [1], Jae-Hyun Noh [1], Da-Young Kim [2], Yong-Sik Chung [1], Tae Hoon Ko [1,]* and Byoung-Suhk Kim [1,]*

[1] Department of Organic Materials & Fiber Engineering, Jeonbuk National University, 567 Baekje-daero, Deokjin-gu, Jeonju-si, Jeollabuk-do 54896, Republic of Korea; gamm7281@naver.com (Y.H.C.); jaeging2@daum.net (J.G.S.); nun20@naver.com (J.H.N); psdcolor@jbnu.ac.kr (Y.S.C.)

[2] Department of Polymer Nano Science & Technology, Jeonbuk National University, 567 Baekje-daero, Deokjin-gu, Jeonju-si, Jeollabuk-do 54896, Republic of Korea; xxnn9@naver.com (D.Y.K.)

* Correspondence: taehoon222@naver.com (T.H.K.); kbsuhk@jbnu.ac.kr (B.S.K.); Tel.: +82-063-270-2352 (T.H.K. & B.S.K.)

Abstract: In this work, we report the carbon fiber-based wire-type asymmetric supercapacitors (ASCs). The highly conductive carbon fibers were prepared by the carbonized and graphitized process using the polyimide (PI) as a carbon fiber precursor. To assemble the ASC device, the $CoMnO_2$-coated and Fe_2O_3-coated carbon fibers were used as the cathode and the anode materials, respectively. FE-SEM analysis confirmed that the $CoMnO_2$-coated carbon fiber electrode exhibited the porous hierarchical interconnected nanosheet structures, depending on the added amounts of ammonium persulfate (APS) as an oxidizing agent, and Fe_2O_3-coated carbon fiber electrode showed a uniform distribution of porous Fe_2O_3 nanorods over the surface of carbon fibers. The nanostructured $CoMnO_2$ were directly deposited onto carbon fibers by a chemical oxidation route without high temperature treatments. In particular, the electrochemical properties of the $CoMnO_2$-coated carbon fiber with the concentration of 6 mmol APS presented the enhanced electrochemical activity, probably due to its porous morphologies and good conductivity. Further, to reduce the interfacial contact resistance as well as improve the adhesion between transition metal nanostructures and carbon fibers, the carbon fibers were pre-coated with the Ni layer as a seed layer using an electrochemical deposition method. The fabricated ASC device delivered a specific capacitance of 221 F g^{-1} at 0.7 A g^{-1} and good rate capability of 34.8% at 4.9 A g^{-1}. Moreover, the wire-type device displayed the superior energy density of 60.16 Wh kg^{-1} at a power density of 490 W kg^{-1} and excellent capacitance retention of 95% up to 3,000 charge/discharge cycles.

Keywords: carbon fiber; wire-type; $CoMn_3O_4$; supercapacitor electrodes

1. Introduction.

In recent years, many researches of the energy storage devices are proceeded to overcome the severe environmental pollution from the fossil fuels. In this case, the energy storage devices, such as Li ion batteries (LIBs) and supercapacitors (SCs) are becoming more and more important [1-3]. In particular, SCs are the most promising energy storage device owing to their higher power densities, longer cycle life, non-toxic nature, and low-cost maintenance compared to the LIBs. The pseudocapacitors based on transition-metal oxides can store and release the charges via the reversible redox reactions of metal oxide's surface and inner sites [4,5]. Indeed, mixed transition metal oxides and hydroxides have been attracted great attention, due to their higher specific capacitance and excellent energy densities. So far, the electrode design of the pseudocapacitors with hierarchically nanostructured and battery-type bimetal oxides has been most important issues to improve the capacitance and energy density [6]. Nevertheless, there is still limitation for a practical application of the supercapacitors to further improve the energy and power densities, rate capability, and cycle lifetime, etc by maintaining its other electrochemical properties [7].

Recently, fiber-type flexible supercapacitors have been extensively studied due to the fast and steady progress in the portable/wearable electronics [8,9]. Till now, one-dimensional supercapacitors have been mostly studied based on fiber/yarn, cable, and wire as a current collector because of the high flexibility, small size, lightweight, and easy to fabricate in wearable devices [10,11]. However, intensive researches are still required to further improve the performances of the fiber-based supercapacitors, such as energy and power densities, rate capability, and life span. Mostly, polymeric fibers [12,13] and carbon fibers [14-16] were used as a substrate to produce the fiber-type flexible supercapacitor devices, while nanocarbon materials (carbon nanotube,[12,17,18] graphene,[19,20] etc), transition metal oxides ($NiCo_2O_4$, MnO_2, Fe_3O_4) [7,15,33] and conductive polymers (polyaniline [13], PEDOT [21,22], Polypyrrole [16]) were used as electroactive materials.[15,23-25] Most of studies have been devoted to solve the problems of lower capacitances and higher internal resistances between active materials and fiber-type electrodes, which can generally reduce the electrochemical performances for a practical application [26,27].

Here, we have used highly conductive carbon fibers as a wire-type electrode, which were prepared by the carbonized and graphitized process using the polyimide (PI) as a carbon fiber precursor [28]. Briefly, the PI fibers were prepared by the wet spinning of polyamic acid and subsequent thermal imidization. The PI fibers were carbonized and finally graphitized at 2,200 ^{o}C. Afterwards, the nanostructured $CoMnO_2$ were directly deposited onto carbon fibers by a chemical oxidation route without high temperature treatments. Further, to reduce the interfacial contact resistance as well as improve the adhesion between transition metal nanostructures and carbon fibers, the carbon fibers were pre-coated with the Ni layer as a seed layer using an electrochemical deposition method. The assembled wire-type asymmetric supercapacitor device using $CoMn_3O_4$-coated carbon fibers as the cathode and Fe_2O_3-coated carbon fibers as the anode materials delivered a specific capacitance of 221 F g^{-1} at 0.7 A g^{-1} and good rate capability of 34.8% at 4.9 A g^{-1}. The fabricated wire-type flexible supercapacitor device displayed the superior energy density of 60.16 Wh kg^{-1} at a power density of 490 W kg^{-1} and excellent capacitance retention of 95% up to 3,000 charge/discharge cycles.

2. Materials and Methods

2.1 Materials

Poly(amic acid) (PAA composed of pyromellitic dianhydride (PDMA)/4,4′-diaminodiphenyl ether (4,4′-ODA), 230,000 cPs of viscosity, SKC Kolon PI Co., Ltd., Republic of Korea)-based carbon fibers (PICFs) [28] were kindly provided by Dissol Inc., Republic of Korea. Cobalt(II) acetate tetrahydrate ($Co(CH_3COO)_2{\cdot}4H_2O$), manganese(II) acetate tetrahydrate ($Mn(CH_3COO)_2{\cdot}4H_2O$), iron(Ⅲ) chloride hexahydrate($FeCl_3{\cdot}6H_2O$), nickel(II) chloride hexahydrate ($NiCl_2{\cdot}6H_2O$), ammonium persulfate (APS, $(NH_4)_2S_2O_8$)) and ammonium chloride (NH_4Cl) were purchased from Sigma Aldrich. All the reagents were an analytical grade and without further purification. All aqueous solutions used in these experiments were prepared with deionized (DI) water (18.2 MΩ·cm, Elga DI water system).

2.2 Fabrication of transition metal oxides-coated PICF electrodes

At first, 4.5mmol $Co(CH_3COO)_2{\cdot}4H_2O$ and 4.5mmol $Mn(CH_3COO)_2{\cdot}4H_2O$ were dissolved in 30ml of DI water and stirred for 1h to make a clear bright red solution. Then the PICF was immersed in the above solution and sonicated slightly to remove the microbubbles of the solution. Afterwards, APS solution with various concentrations of 1, 3, 6, and 9 mmol was further added and reacted at $60^{o}C$ for 12h (via chemical oxidation) and labelled as $CoMnO_2$@PICF-1, $CoMnO_2$@PICF-3, $CoMnO_2$@PICF-6 and $CoMnO_2$@PICF-9, respectively. The obtained $CoMnO_2$-decorated PICFs ($CoMnO_2$@PICFs) as cathode material was washed with DI water gently, and dried at 60 ^{o}C. The mass loading of $CoMnO_2$ metal oxide deposited onto PICF was about 2 mg. For the preparation of anode material, 6 mmol $FeCl_3{\cdot}6H_2O$ was dissolved in 60 ml of DI and stirred for 1hr at room temperature to make a homogeneous solution. Then, PICF and the above solution were transferred into a 80 ml Teflon-lined stainless steel autoclave, and then hydrothermal treatment was carried out at $140^{o}C$ for 12 h in a oven. The resultant product was carefully rinsed with DI and dried at $60^{o}C$ for 12 h. Finally, the obtained sample was calcinated at $350^{o}C$ for 2h at a heating rate of $2^{o}C$ min^{-1} to achieve the Fe_2O_3-decorated PICF (Fe_2O_3@PICF). The mass loading of coated Fe_2O_3 metal oxides was about 1 mg.

2.3 Electrodeposition of Ni seed layer on PICF

For the deposition of Ni seed layer, 2M NH_4Cl and 0.1M $NiCl_2{\cdot}6H_2O$ as the supporting electrolyte were dissolved in 100ml of DI water, and used as the solution from which electrodeposition was performed. The PICF and Pt wire were used for working and reference electrodes, respectively. The Ni seed layer deposition was carried out with a constant current density of 0.25 A cm^{-2} (by adjusting 7V and 0.5A) at a deposition time of 20s (denoted as Ni20@PICF) using a DC power supply. After deposition, the samples were washed with DI and dried at 60°C for 12 h. The schematic illustration for the preparation of $CoMnO_2$@PICFs was represented in Schematic 1.

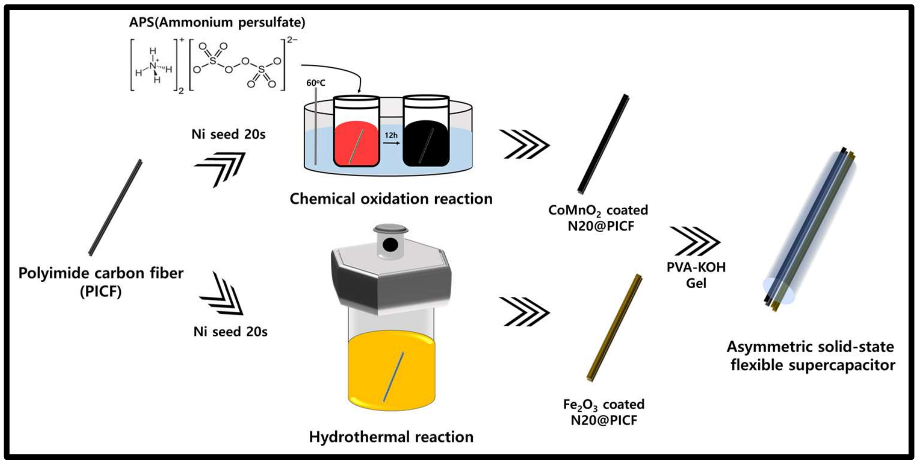

Scheme 1. Schematic illustration for the preparation of a wire-type asymmetric supercapacitor by using $CoMn_3O_4$- and Fe_2O_3-coated carbon fibers as cathode and anode materials.

2.5 Characterization

The surface morphologies were examined by field emission scanning electron microscopy (FE-

SEM, JEOL JSM-5900) along with energy dispersive X-ray (EDX) system. The X-ray diffraction studies were performed using Rigaku diffractometer, CuK$_\alpha$ radiation operating at 40 keV/40 mA at a scanning rate of 15° per min in the 2θ ranges from 10° to 80°. The chemical state of the element linked with the surface chemical composition of the sample was analyzed by X-ray photoelectron spectroscopy (XPS, ESCALAB250, Al Ka radiation).

2.6 Electrochemical measurements

The electrochemical performance was investigated by cyclic voltammetry (CV), electrochemical impedance spectroscopy (EIS) and galvanostatic charge-discharge (GCD). The CV and EIS measurements were carried out in a three-electrode system at room temperature using an electrochemical workstation (Princeton Applied Research, Versatat 4). Here, Pt wire was used as the counter electrode, Ag/AgCl as the reference electrode and the prepared samples as the working electrode, respectively. The CV curves were recorded within the potential window from 0 to 0.6 V [vs. Ag/AgCl] in 1M KOH electrolyte at various scan rates (5, 10, 20, 50 and 100 mV s^{-1}). The GCD tests were carried out within the potential range of 0 to 0.5 V in 1M KOH. The specific capacitance of the fabricated electrodes was calculated from the discharge curves using the following equation (1),

$$C = I\Delta t / m\Delta V \tag{1}$$

where, C is the specific capacitance (F g^{-1}), I is the discharge current (mA), m is the mass (mg) of the electroactive material, Δt and ΔV are the discharge time (s) and potential window (V). The EIS measurement was carried out at open circuit potential in the frequency range of 0.1 Hz to 100 kHz. The ZView software was employed to fit the EIS data. The impedance data are presented in the form of Nyquist plot. The values of the charge transfer resistance (R_{CT}) and internal resistance (R_S) of the electrodes were determined using Zsimpwin software simulations.

For the practical applications, the asymmetric supercapacitor (ASC, $CoMnO_2$/N20@PICF//Fe_2O_3/N20@PICF) device was constructed using $CoMnO_2$/N20@PICF and Fe_2O_3/N20@PICF as positive electrode and negative electrode materials, respectively. The PVA/KOH gel electrolyte was used for electrolyte and separator in this ASC device. To prepare the PVA/KOH gel electrolyte, 2g PVA and 2g KOH were added to the 20ml DI water and it was kept under stirring and then heated slowly to 90^{o}C until it became clear and transparent. After it was cooled down to room temperature, the $CoMnO_2$/N20@PICF and Fe_2O_3/N20@PICF electrodes were coated with PVA/KOH gel electrolyte and carefully assembled together and then sealed in the plastic tube to fabricate the wire-type ASC device. To obtain optimum energy and power densities, the optimal mass ratio of both electrodes was determined based on the charge balance relationship (q^+ and q^- are the charges acquired by the cathode and anode materials) provided by the following equation (2),

$$m^+ / m^- = (C_m^- \circledcirc V^-) / (C_m^+ \circledcirc V^+) \tag{2}$$

where m^+, m^-, C_m^+, C_m^-, V^+, and V^- signifies the mass (g), specific capacitance (F g^{-1}) and working potential window (V) for the cathode and anode materials. The energy (E, Wh kg^{-1}) and power densities (P, W kg^{-1}) of as-assembled ASC device were computed by equations (3) and (4), respectively.

$$E = C_{sp} \times \Delta V^2 / 2 \times 3.6 \tag{3}$$

$$P = E \times 3600/\Delta t \tag{4}$$

where C_{sp} indicates the specific capacitance of ASC device (F g^{-1}), ΔV is the working potential window (V) and Δt is the discharging time (s).

3. Results and Discussion

Figure 1 presents the FE-SEM images of pure PICF (a, b), $CoMnO_2$@PICF-1 (c, d), $CoMnO_2$@PICF-3 (e, f), $CoMnO_2$@PICF-6 (g, h) and $CoMnO_2$@PICF-9 (i, j), respectively. It can be clearly seen that hierarchical $CoMnO_2$ nanostructures were successfully formed on the surface of PICFs. While the bare PICFs showed smooth surface morphologies, $CoMnO_2$@PICFs exhibited the porous hierarchical interconnected nanosheet structures, which depended on the added amounts of APS. Insets in Figures 1d, 1f, 1h and 1j show the higher magnified SEM images. We have also measured the elemental mapping and corresponding EDX spectrum using FE-SEM equipped with EDX measurement (Figure 1k). The results confirmed the presence of C, Co, Mn, O elements, supporting the successful deposition of $CoMnO_2$ onto PICFs.

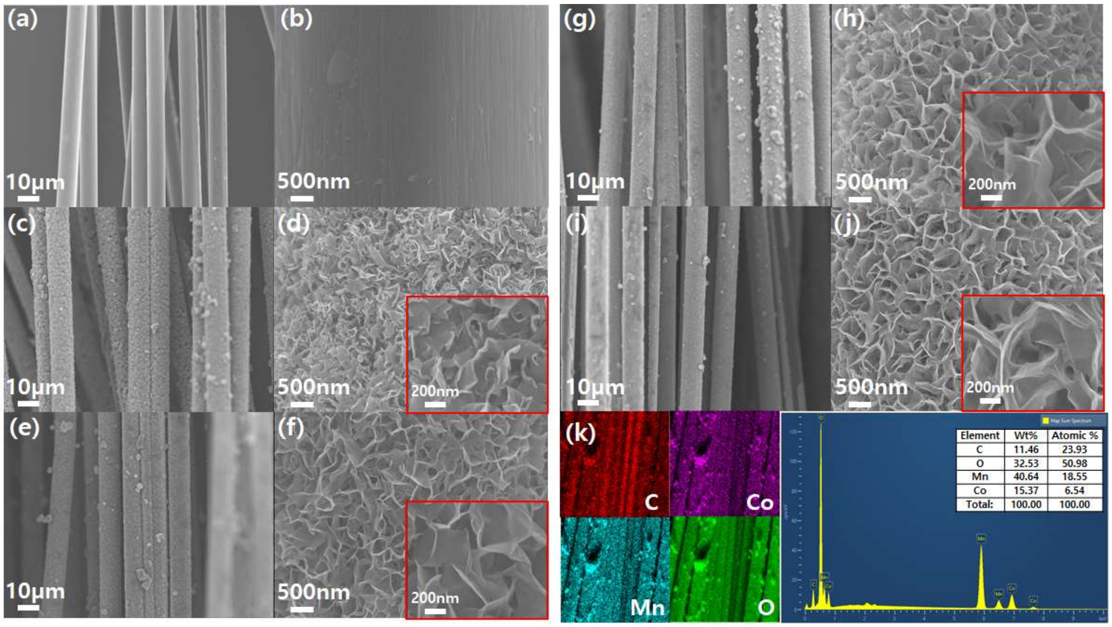

Element	Wt%	Atomic %
C	11.46	23.93
O	32.53	50.98
Mn	40.64	18.55
Co	15.37	6.54
Total:	100.00	100.00

Figure 1. FE-SEM images of pure PICF (a, b), $CoMnO_2$@PICF-1 (c, d), $CoMnO_2$@PICF-3 (e, f), $CoMnO_2$@PICF-6 (g, h) and $CoMnO_2$@PICF-9 (i, j), and inset shows the higher magnified images. The elemental mapping and EDX spectrum (k) of $CoMnO_2$@PICF-6.

Electrochemical properties of the fabricated $CoMnO_2$@PICFs electrodes was investigated via CV and GCD methods in 1M KOH electrolyte solution. Figure. 2a presents CV curves of pure PICFs, $CoMnO_2$@PICF-1, $CoMnO_2$@PICF-3, $CoMnO_2$@PICF-6 and $CoMnO_2$@PICF-9 at the scan rate of 20 mV s^{-1} within the potential window 0.0 to +0.6 V vs. [Ag/AgCl]. The shapes of CV curves for $CoMnO_2$@PICFs were nearly rectangular. No redox peaks were clearly detected on the CV curves for the $CoMnO_2$@PICFs electrodes, attributed to the fast, reversible successive surface redox reactions [29]. Moreover, it clearly showed that the integrated area of $CoMnO_2$@PICF-6 was larger than $CoMnO_2$@PICF-1, $CoMnO_2$@PICF-3 and $CoMnO_2$@PICF-9, suggesting feasible enhancement in the electrochemical activity, probably due to its porous morphology and good conductivity. On the other

doi:10.20944/preprints202011.0004.v1

hand, the contribution of pure PICFs to the capacitance was almost negligible, as seen in Figure 2a, suggesting that the added $CoMnO_2$ enhanced the capacitance significantly. Further, the CV curves of $CoMnO_2$@PICFs remained unchanged, as increasing the scan rate, indicating the excellent electrochemical reversibility (Figure S1), which is one of important parameters in the pseudocapacitive electrodes. Moreover, the CV curves well maintained symmetrical shape, demonstrating the reversible electrochemical redox reaction and excellent rate capability of the electrode material [30].

Capacitive performance of the $CoMnO_2$@PICFs electrodes was further studied by the GCD measurements at the current density of 1 A g^{-1} within the potential range from 0 to +0.5V (Figure 2b). The fabricated $CoMnO_2$@PICF-1, $CoMnO_2$@PICF-3, $CoMnO_2$@PICF-6 and $CoMnO_2$@PICF-9 electrodes delivered the specific capacitances of 362, 634, 928, 688 F g^{-1} at the current density of 1 A g^{-1}, respectively. Figure 2c shows the relationship of specific capacitance vs. current density of the $CoMnO_2$@PICF electrodes with different amounts of APS. The highest specific capacitance (~928 F g^{-1}@1 A g^{-1}) of the $CoMnO_2$@PICF-6 electrode was about 2.56, 1.46 and 1.34 times higher than those of the $CoMnO_2$@PICF-1 (~362 F g^{-1}@1 A g^{-1}), $CoMnO_2$@PICF-3 (~643 F g^{-1}@1 A g^{-1}) and $CoMnO_2$@PICF-9 (~688 F g^{-1}@1 A g^{-1}) electrodes at the current density of 1.0 A g^{-1}, respectively, and also the capacitance decreased to 270 F g^{-1} at 5 A g^{-1}. The capacitance decreased by 29 % at higher current density, proving the excellent high-rate capability. The EIS was exploited to investigate the ion diffusion and electron transfer of the $CoMnO_2$@PICF electrodes. Figure 2d presents the Nyquist plots for the pure PICF, $CoMnO_2$@PICF-1, $CoMnO_2$@PICF-3, $CoMnO_2$@PICF-6 and $CoMnO_2$@PICF-9 electrodes in the frequency range of 0.1 to 100 kHz with an amplitude of 10 mV. The EIS spectrum was composed of a small semicircle in a high-frequency range and a linear curve in the low-frequency range. The internal resistance (R_S) is the sum of the ionic resistance of the electrolyte. The intrinsic resistance of the active material and the contact resistance at the active material/current collector interface can be derived from the intercept of the plots on the real axis. The semicircle of Nyquist plot corresponds to the Faradic reaction and its diameter represents the interfacial charge transfer resistance (R_{CT}) [31]. The fabricated $CoMnO_2$@PICFs electrodes showed a semicircle at higher frequency region, and the inset showed magnified higher frequency region. The calculated R_{CT} values were 11.69Ω, 27.11Ω, 14.05Ω and 23.75Ω for the $CoMnO_2$@PICF-1, $CoMnO_2$@PICF-3, $CoMnO_2$@PICF-6 and $CoMnO_2$@PICF-9 electrodes, respectively. The values were tabulated in inset of figure. As a result, it was found that the $CoMnO_2$@PICF-6 showed best electrochemical activity. Although the value of R_{CT} (14.05Ω) of the $CoMnO_2$@PICF-6 electrode was a rather large, we could see the lower R_S value (9.19Ω) of the $CoMnO_2$@PICF-6 electrode at the intersection of the real axis, indicating a low internal resistance.

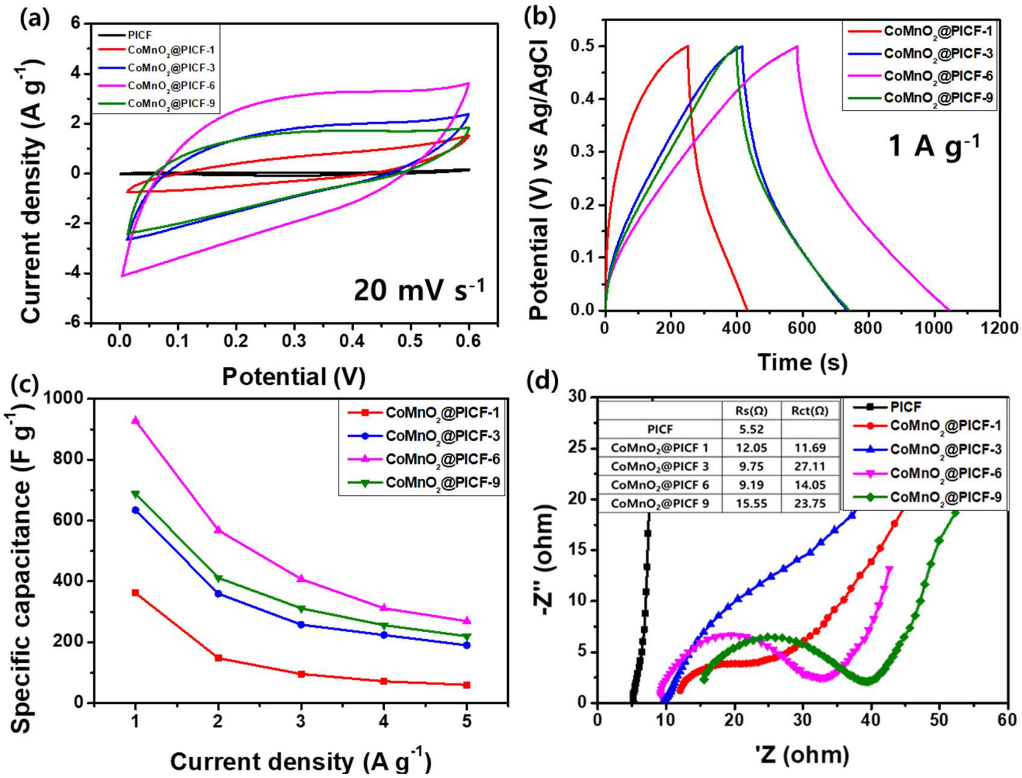

	Rs(Ω)	Rct(Ω)
PICF	5.52	
CoMnO$_2$@PICF 1	12.05	11.69
CoMnO$_2$@PICF 3	9.75	27.11
CoMnO$_2$@PICF 6	9.19	14.05
CoMnO$_2$@PICF 9	15.55	23.75

Figure 2. CV curves (a), GCD curves (b), relationship between capacitance and current density (d), and EIS curves (d) of pure PICFs, CoMnO$_2$@PICF-1, CoMnO$_2$@PICF-3, CoMnO$_2$@PICF-6 and CoMnO$_2$@PICF-9.

In order to further improve the interfacial properties of the fabricated CoMnO$_2$@PICFs electrode, the additional Ni as a seed layer was deposited on the PICF electrode before CoMnO$_2$ deposition. Figure 3 shows the FE-SEM images of pure PICF (a), N10@PICF (b), N20@PICF (c) and CoMnO$_2$/N20@PICF-6 (d), respectively. This result indicated that N20@PICF showed evenly Ni-coated and rather smooth surface morphology (Figure 3c), while N10@PICF clearly showed poor coverage of Ni on PICF (Figure 3b). Furthermore, CoMnO$_2$/N20@PICF-6 showed the similar surface morphology to the CoMnO$_2$@PICF-6 (Figure 3d). We have further checked the crystal structure of pure PICF, N20@PICF, CoMnO$_2$@PICF-6 and CoMnO$_2$/N20@PICF-6 by XRD (Figure 4a). The bare PICF showed a broad peak around 25.4°, corresponding to the graphitic carbon peak [32]. The Ni20@PICF showed the additional diffraction peaks at 44.6°, 52.0°, and 76.7°, which were well indexed to (111), (200), and (220) crystal planes, respectively, suggesting the 3D-Ni metal skeleton [33] as well as face-centered cubic structure of nickel/nickel oxide (JCPDS No. 87-0712) [34]. The CoMnO$_2$-decorated both PICF-6 and N20@PICF-6 showed the diffraction peaks at 12.2°, 18.9°, 36.8°, 38.3°, 42.7° and 65.9°, which were well indexed to the (110), (111), (311), (222), (301) and (440) crystal planes, respectively. Among them, the diffraction peaks at 12.2 ° and 42.7 ° were indexed to the characteristic (110) and (301) crystal planes of α-MnO$_2$ [JCPDS No. 44-0141] [35]. The peaks at 18.9°, 36.8°, 38.3° and 65.9° were well indexed to the characteristic (111), (311), (222), and (440) crystal planes of Co$_3$O$_4$ [JCPDS No. 43-1003] [36]. The results demonstrated the successful coating of CoMnO$_2$ with amorphous phase [37].

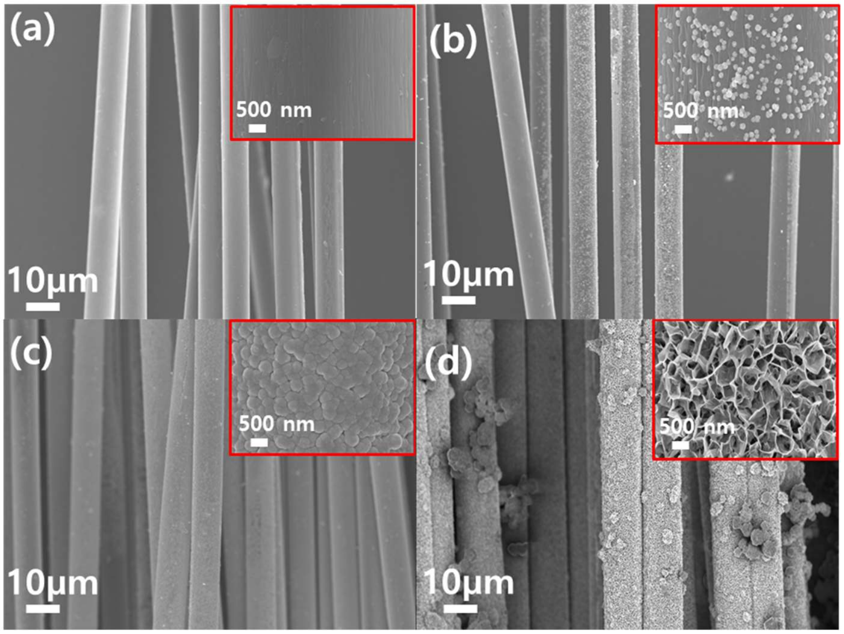

Figure 3. FE-SEM images of pure PICF (a), N10@PICF (b), N20@PICF (c) and CM/N20@PICF-6 (d), inset shows the higher magnified images.

To confirm the chemical states of $CoMnO_2$/N20@PICF-6, XPS studies were carried out (Figures 4b-4f). The survey spectrum shows the presence of Ni, Co, Mn, O and C without other impurity elements. The observed Ni peak is ascribed to the Ni seed layer on the PICF. The deconvoluted Co 2p spectrum suggested the existence of $Co^{(0)}$, Co^{2+}, and Co^{3+} at the 778.5-795.1 eV, 780.5 eV and 779.5-797.3 eV, respectively. The deconvoluted Mn 2p spectrum displayed two peaks at 653.9 and 642.2 eV, which were ascribed to the presence of mixed Mn $2p^{1/2}$ and Mn $2p^{3/2}$ with a spin-energy separation of 11.7eV. The O 1s spectrum at 529.5 eV, 531.58 eV and 533.28 eV can be attributed to metal oxygen bond (M-O, M-Co, Mn), the hydrated trivalent oxide bond (M-O-H), and the residual water bond (H-O-H), respectively. In the C 1s spectrum of $CoMnO_2$@PICFs, the sharp peak at around 286 eV can be spilt to three peaks at 284.4, 286.6, and 288.9 eV, which represent the sp^2 graphitic carbon, C–O and O–C=O bonds. The Co and Mn contents of $CoMnO_2$/N20@PICFs reached 15.87 and 14.57 atomic%, suggesting the successful formation of $CoMnO_2$ on the fiber substrate.

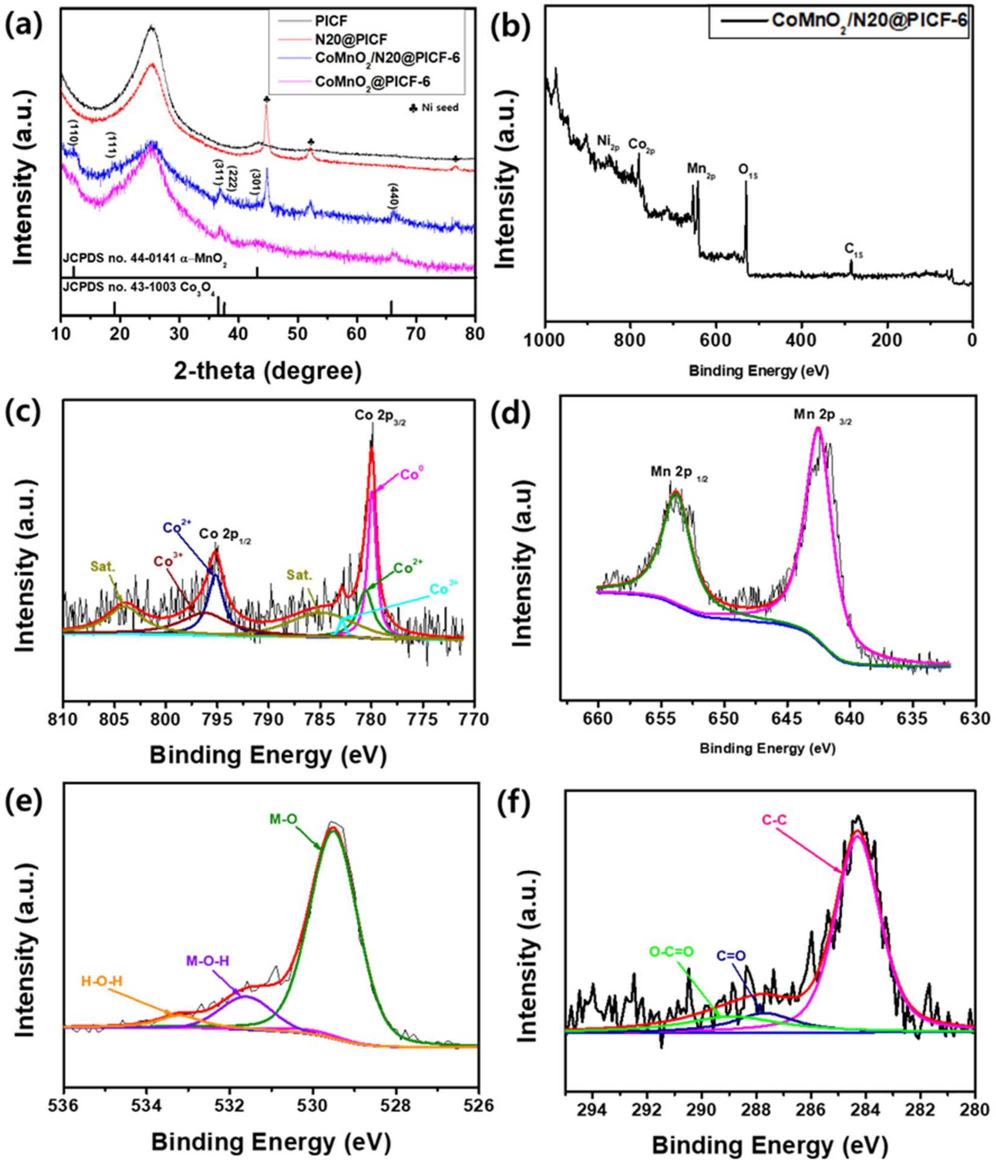

Figure 4. XRD patterns (a) of pure PICF, N20@PICF, $CoMnO_2$@PICF-6 and $CoMnO_2$/N20@PICF-6. The XPS survey spectrum (b) of $CoMnO_2$/N20@PICF-6 and XPS spectra of Co 2p (c), Mn 2p (d), O 1s (e), C 1s (f) for $CoMnO_2$/N20@PICF-6 in high resolution.

In order to investigate the effect of Ni seed layer on the electrochemical properties of $CoMnO_2$@PICF-6, CV and EIS tests of bare PICF, $CoMnO_2$@PICF-6, and $CoMnO_2$/N20@PICF-6 were carried out in three-electrode configuration. As seen in Figure 5a, the $CoMnO_2$/N20@PICF-6 electrode showed clearly broader and large integrated area than those of other samples, suggesting an enhanced electrochemical storage ability. As expected, the $CoMnO_2$/N20@PICF-6 displayed the longer discharge time (Figure 5b), as compared to the $CoMnO_2$@PICF-6. The specific capacitances calculated from the discharge curves were plotted as a function of current density (Figure 5c). The $CoMnO_2$/N20@PICF-6 electrode delivered excellent specific capacitances of 1206, 996, 876, 776, 700, 624, 574, 512, 468 and 420 F g^{-1} at the current densities of 1, 2, 3, 4, 5, 6, 7, 8, 9 and 10 A g^{-1}, respectively, which were clearly higher than those of the $CoMnO_2$@PICF-6 and even Ni20@PICF electrodes. The electrochemical performances of the $CoMnO_2$-decorated PICF electrodes ($CoMnO_2$@PICF-6, $CoMnO_2$/N20@PICF-6) were further investigated by EIS. Except for Ni20@PICF, the $CoMnO_2$/N20@PICF-6 showed the lower R_{CT} value (3.43Ω), suggesting that Ni seed layer provided a good interfacial contact between $CoMnO_2$ and PICF, giving the lower interfacial resistance and a fast reversible redox reaction.

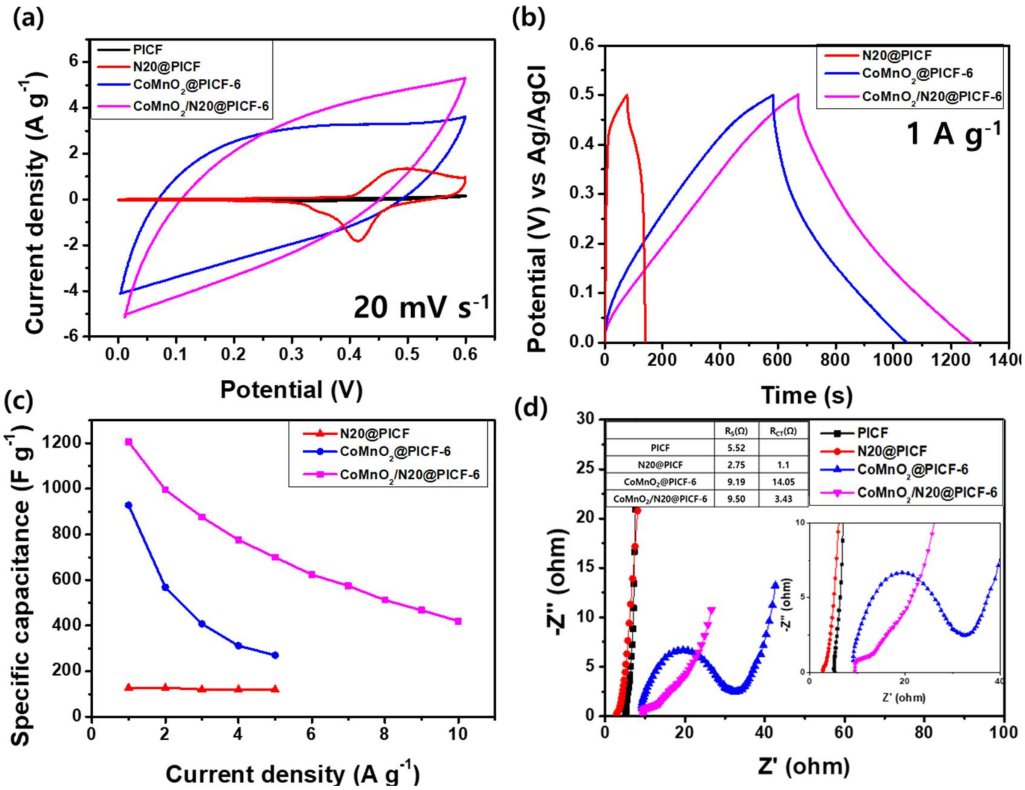

	R_S(Ω)	R_{CT}(Ω)
PICF	5.52	
N20@PICF	2.75	1.1
$CoMnO_2$@PICF-6	9.19	14.05
$CoMnO_2$/N20@PICF-6	9.50	3.43

Figure 5. CV curves (a), GCD curves (b), specific capacitance vs. current density (c), Nyquist plot (d) of bare PICF, N20@PICF, $CoMnO_2$@PICF-6 and $CoMnO_2$/N20@PICF-6.

To further evaluate the real capacitance of the fabricated electrodes, an ASC full-cell was assembled with cathode and anode materials. To fabricate the full-cell, Fe_2O_3-decorated N20@PICF with Ni seed layer (Fe_2O_3/N20@PICF) prepared by hydrothermal method was used as anode material. FE-SEM image showed a uniform distribution of porous Fe_2O_3 nanorods over the surface of PICF, as can be seen in inset of Figure 6a. Figure 6b shows the survey XPS spectrum of Fe_2O_3/N20@PICF sample which contained Fe, O, Ni and C elements. The Fe 2p spectrum (Figure 6c) exhibited two distinct peaks of Fe $2p^{1/2}$ and Fe $2p^{3/2}$ at the binding energies of 724.58 and 710.9 eV, respectively. Moreover, two satellite peaks were also observed, indicating the existence of Fe^{3+} in Fe_2O_3 [38]. Figure 6d presents the XPS spectra of O 1s level of the sample. The peak can be deconvoluted into two peaks at 529.78 and 531.58 eV. The peak at 529.78 eV was due to the lattice oxygen of the Fe_2O_3, and the other peak at the 531.58 eV the presence of other components such as OH, H_2O, and carbonate species adsorbed onto the surface [39].

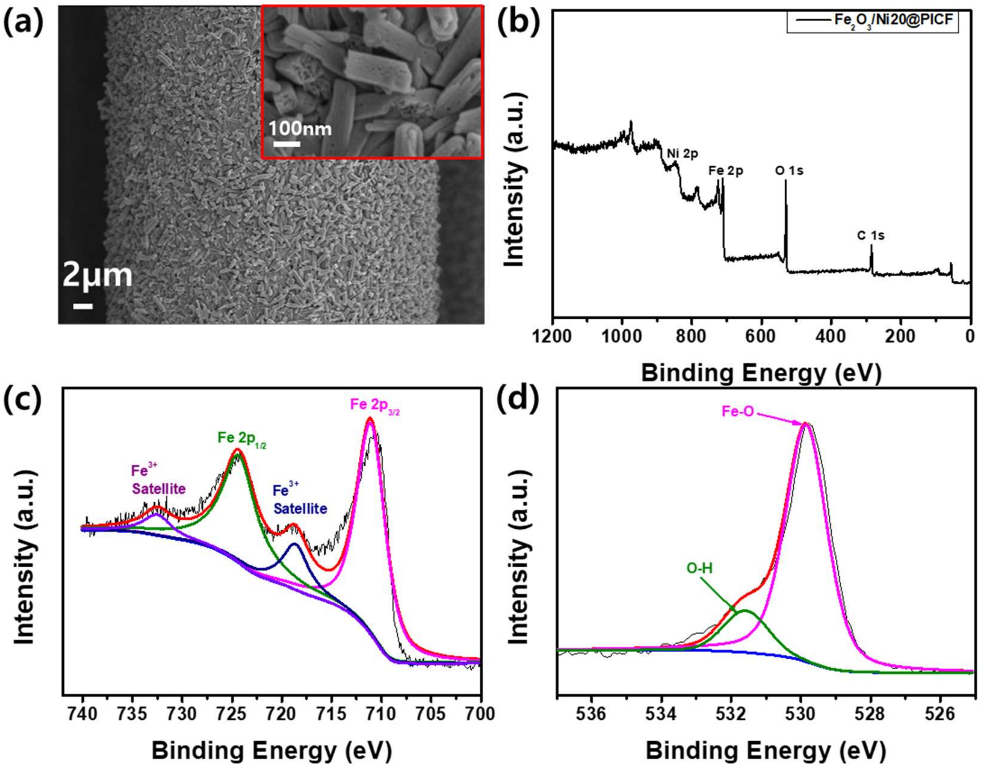

Figure 6. FE-SEM image (a), XPS survey spectrum (b) and XPS spectra of Fe 2p (c), O 1s (d) for Fe_2O_3/N20@PICF in high resolution.

To test the feasibility of the $CoMnO_2$/N20@PICF-6 and Fe_2O_3/N20@PICF electrodes for a real application, we have assembled the ASC device by sandwiching the $CoMnO_2$/N20@PICF-6 as a cathode and Fe_2O_3/N20@PICF as an anode material with PVA-KOH as a polymer electrolyte. The optimal mass ratio (m^+ /m^-) of the cathode and anode materials was calculated by using equation (2), and it turned out to be 1 : 0.7. The CV profiles of the $CoMnO_2$/N20@PICF6 and Fe_2O_3/N20@PICF electrodes were shown in Figure 7a. The potential windows of the anode and cathode materials were -1.0-0 V and 0-0.6 V, respectively. Accordingly, the maximum operation potential for the wire-type ASC device was anticipated to reach 1.5 V. The typical CV curves of the ASC device in a potential window of 0.0-1.5 V at different scan rates were presented in Figure 7b. It displayed a rectangular-like shape, indicating that the device showed a fast charge/discharge behavior and high rate ability. The triangular-shaped GCD curves in Figure 7c revealed the satisfactory electrochemical reversibility and capacitive characteristics of the ASC device. The calculated specific capacitance was 221 F g^{-1} at the current density of 0.7 A g^{-1}. Moreover, the capacitance value started to decrease as the current density further increased. The ASC device showed stable electrochemical performances at different voltage windows. As seen in Figure 7d, the CV profiles collected at 20 mV s-1 remained rectangular-like shape upto 1.5V. The charge-discharge profiles at different ranges of voltage at 1.4 A g^{-1} also exhibited triangular-shaped curves upto 1.4 V (Figure 7e). With the extension of voltage windows, the calculated electrical performance of the device slightly increased from 159.6 F g^{-1} to 177 F g^{-1}. The Nyquist plot (Figure 7f) shows an estimated R_S and R_{CT} values of 23.2 Ω and 16.86 Ω, respectively, which derived from the low resistance of the conductive carbon fiber substrate and the compact cell assembly. At low frequencies, the ASC device showed vertical behavior, which indicates that samples possess capacitor characteristics. Thus the ASC device had good capacitive properties. Furthermore, the $CoMnO_2$/N20@PICF-6//Fe_2O_3/N20@PICF device exhibited higher capacitance retention rate of 95% after 3000 charge/discharge cycles at 2.8 A g^{-1} than that (retention rate of 82%) of the $CoMnO_2$@PICF-6 and Fe_2O_3@PICF device, due to the reduced interfacial contact resistance by a Ni layer introduced (Figure 7g). Also the rate capability was slightly increased by the electrodeposition of Ni seed layer (inset in Figure 7g). In addition, the assembled $CoMnO_2$/N20@PICF-6//Fe_2O_3/N20@PICF device delivered a maximum specific energy density of 60.16 Wh kg^{-1} at power density of 490 W kg^{-1}, as shown by Ragone plot (Figure 7h). Compared to other devices, these values were higher than other energy storage devices, such as NiCoMn-TH/AEG//CFP-S (23.5 Wh kg^{-1} at 427 W kg^{-1}) [40], NiCoMn-OH//AC (43.2 Wh kg^{-1} at 790W kg^{-1}) [41], CoMn-HW/RGO10//AC (38.3 Wh kg^{-1} at 8000 W kg^{-1}) [42], CoMn LDH/PPy//MLG (29.6 Wh kg^{-1} at 500 W kg^{-1}) [43], NCM//AC (23.7 Wh kg^{-1} at 2625 W kg^{-1}) [44], Ni-Mn LDH/rGO//AC (33.8 Wh kg^{-1} at 850 W kg^{-1}) [45], and Co/Mn-ZIF//AC (52.5 Wh kg^{-1} at 1080 W kg^{-1}) [46], as summarized in Table S1. Therefore, the fabricated wire-type ASC device exhibited the excellent electrochemical performance with good electrical conductivity.

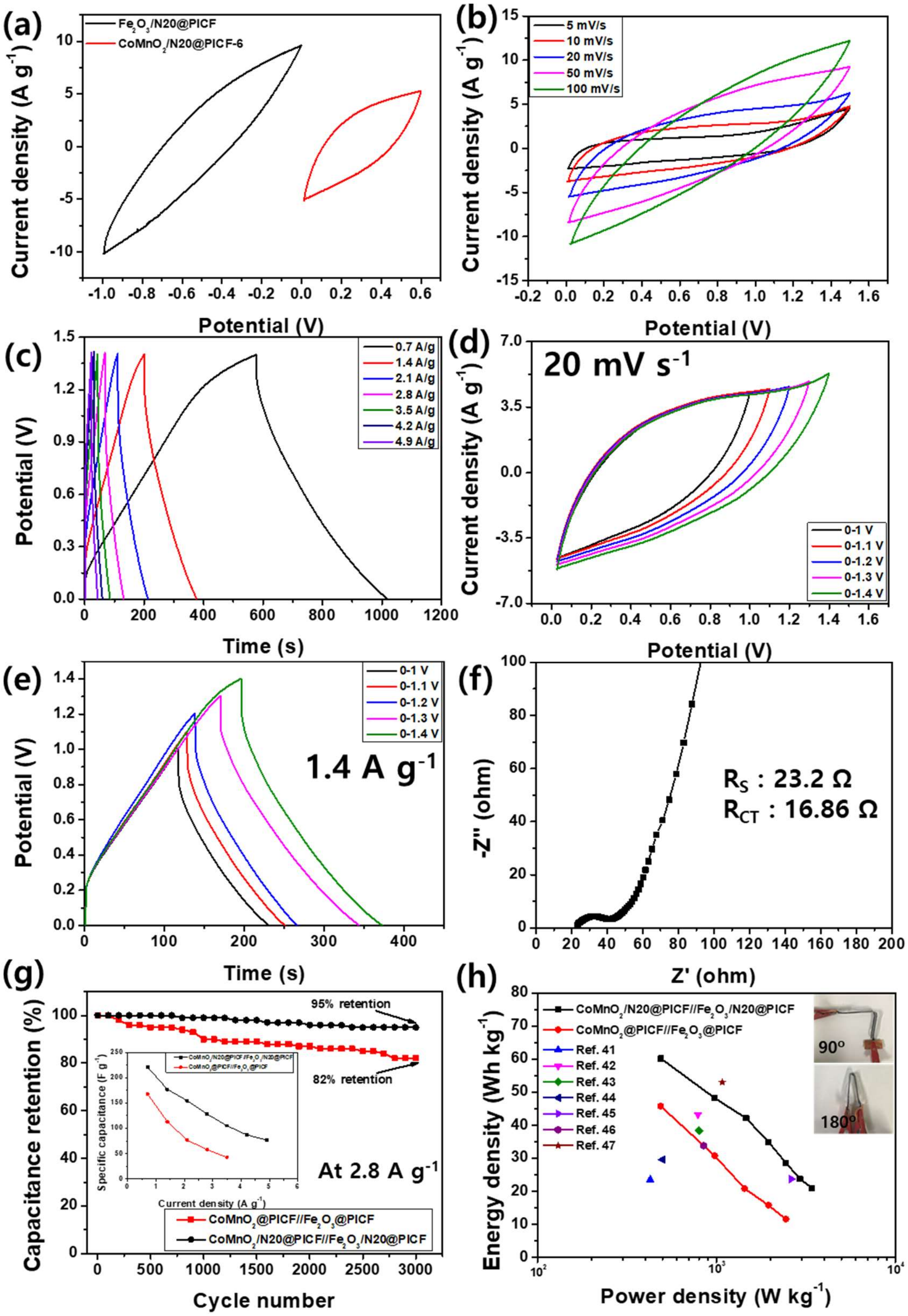

Figure 7. CV curves (a) of the cathode and anode materials at 20 mV s^{-1}, CV curves (b) of the ASC device at various scan rates, GCD curves (c) of the ASC device at different currents density, CV curves (d) at different potential windows at 20 mV s^{-1}, GCD curves (e) at different potential windows at 1.4 A g^{-1}, Nyquist plot (f) of the ASC device, cycle performance (g) of the ASC device for 3000 cycles at 2.8 A g^{-1} (inset shows the relationship between specific capacitance and current density of the ASC device), (h) Ragone plot (inset shows the digital images of the ASC device upon bending).

Supplementary Materials: The following are available online at www.mdpi.com/xxx/s1, Figure S1: CV curves of pure PICFs, $CoMnO_2$@PICF-1, $CoMnO_2$@PICF-3, $CoMnO_2$@PICF-6 and $CoMnO_2$@PICF-9 electrode materials at various scan rates, Table S1: The specific capacitance, energy density and cycle stability of the $CoMnO_2$/N20@PICF-6//Fe_2O_3/N20@PICF device, compared to previously reported mixed transition metal oxide based electrode materials.

Author Contributions: Conceptualization, T.H.K. and B.S.K.; methodology, Y.H.C. and J.G.S.; investigation, Y.H.C., J.G.S., J.H.N and D.Y.K.; writing—original draft preparation, Y.H.C., T.H.K. and B.S.K.; writing—review and editing, T.H.K. and B.S.K.; supervision, T.H.K. and B.S.K.; funding acquisition, Y.S.C. and B.S.K. All authors have read and agreed to the published version of the manuscript.

Acknowledgments: This research was funded by the National Research Foundation of Korea (NRF) grant funded by the Korea government (MSIT) (No. 2020R1A2C2012356).

Conflicts of Interest: The authors declare no conflict of interest.

References

1. Wang, L.; Menakath, A.; Han, F.; Wang, Y.; Zavalij, P.Y.; Gaskell, K.J.; Borodin, O.; Iuga, D.; Brown, S.P.; Wang, C.; Xu, K.; Eichhorn, B.W. Identifying the components of the solid-electrolyte interphase in Li-ion batteries. *Nat. Chem*. **2019**. *11*, 789-796.
2. Zhai, S.; Karahan, H.E.; Wang, C.; Pei, Z.; Wei, L.; Chen, Y. 1D supercapacitors for emerging electronics: current status and future directions. *Adv. Mater*. **2020**, *32*, 1902387-1902405.
3. Zeng, Y.; Yu, M.; Meng, Y.' Fang, P.; Lu, X.; Tong, Y. Iron-based supercapacitor electrodes: advances and challenges. *Adv. Energy. Mater.* **2016**, *6*, 1601053-1601069.
4. Zhou, K.; Zhou, W. Yang, L.; Lu, J.; Cheng, S.; Mai, W.; Tang, Z.; Li, L.; Chen, S. Ultrahigh-performance pseudocapacitor electrodes based on transition metal phosphide nanosheets array via phosphorization: a general and effective approach. *Adv. Funct. Mater*. **2015**, *25*, 7530-7538.
5. Ling, T.; Da, P.; Zheng, X.; Ge, B.; Hu, Z.; Wu, M.; Du, .X.W.; Hu, W.B.; Jaroniec, M.; Qiao, S.Z. Atomic-level structure engineering of metal oxides for high-rate oxygen intercalation pseudocapacitance. *Sci. Adv*. **2018**, *4*, eaau6261-eaau6268.
6. Huang, X.; Liu, H.; Zhang, X. Jiang, H. High performance all-solid-state flexible micro-pseudocapacitor based on hierarchically nanostructured tungsten trioxide composite. *ACS. Appl. Mater. Int*. **2015**, *7*, 27845-27852.
7. Ko,T.H.; Lei, D.; Balasubramaniam, S.; Seo, M.K.; Chung, Y.S.; Kim, H.Y.; Kim, B.S. Polypyrrole-decorated hierarchical $NiCo_2O_4$ nanoneedles/carbon fiber papers for flexible high-performance supercapacitor applications. *Electrochim. Acta* **2017**, *247*, 524-534.
8. Chodankar, N.R.; Dubal, D.P.; Ji, S.H.; Kim, D.H. Self-assembled nickel pyrophosphate-decorated amorphous bimetal hydroxides 2D-on-2D nanostructure for high-energy solid state asymmetric supercapacitor. *Small* **2019**, *15***,** 1901145-19001155.
9. Patil, A.M.; Lokhande, A.C.; Chodankar, N.R.; Shinde, P.A.; Kim, J.H.; Lokhande, C.D. Interior design engineering of CuS architecture alteration with rise in reaction bath temperature for high performance symmetric flexible solid state supercapacitor. *J. Ind. Eng. Chem.* **2017**, *46*, 91-102.
10. Meng, F.; Li, Q.; Zheng, L. Flexible fiber-shaped supercapacitors: design, fabrication, and multi-functionalities. Energy Storage Mater. **2017**, *8*, 85-109.
11. Hu, M.; Liu, Y.; Zhang, M.; Wei, H.; Gao, Y. Wire-type MnO_2/Multilayer graphene/Ni electrode for high-performance supercapacitor. *J. Power Sources* **2016**, *335*, 113-120.
12. Yang, Z.; Deng, J.; Chen, X.; Ren, J.; Peng, H. A highly stretchable, fiber-shaped supercapacitor. *Angew. Chem., Int. Ed.* **2013**, *52*, 13453.
13. Devarayan, K.; Lei, D.L Kim, H.Y.; Kim, B.S. Flexible transparent electrode based on PANi nanowire/nylon nanofiber reinforced cellulose acetate thin film as supercapacitor. *Chem. Eng. J.* **2015**, *273*, 603-609.
14. Liu, N.; Ma, W.; Tao, J.; Zhang, X.; Su, J.; Li, L.; Yang, C.; Gao, Y.; Golberg, D.; Bando, Y. Cable-type supercapacitors of three-dimensional cotton thread based multi-grade nanostructures for wearable energy storage. *Adv. Mater.* **2013**, *25*, 4925-4931.
15. Zhai, T.; Xie, S.; Yu, M.; Fang, P.; Liang, C.; Lu, X.; Tong, Y. Oxygen vacancies enhancing capacitive properties of MnO_2 nanorods for wearable asymmetric supercapacitors. *Nano Energy* **2014**, *8*, 255-263.

16. Huang, Y.; Huang, Y.; Zhu, M.; Meng, W.; Pei, Z.; Liu, C.; Hu, H.; Zhi, C. Magnetic-assisted, self-healable yarn-based supercapacitor. *ACS Nano* **2015**, *9*, 6242-6251.
17. Jayaseelan, S.S.; Ko, T.H.; Radhakrishnan, S.; Yang, C.M.; Kim, H.Y.; Kim, B.S. Novel MWCNT interconnected $NiCo_2O_4$ aerogels prepared by a supercritical Co_2 drying method for ethanol electrooxidation in alkaline media. *Int. J. Hydrogen Energy* **2016**, *41*, 13504-13512.
18. Wang, K.; Meng, Q.; Zhang, Y.; Wei, Z.; Miao, M. High-performance two-ply yarn supercapacitors based on carbon nanotubes and polyaniline nanowire arrays. *Adv. Mater.* **2013**, *25*, 1494-1498.
19. Meng, Y.; Zhao, Y.; Hu, C.; Cheng, H.; Hu, Y.; Zhang, Z.; Shi, G.; Qu, L. All-graphene core-sheath microfibers for all-solid-state, stretchable fibriform supercapacitors and wearable electronic textiles. *Adv. Mater.* **2013**, *25*, 2326-2331.
20. Li, X.; Zang, X.; Li, Z.; Li, X.; Li, P.; Sun, P.; Lee, X.; Zhang, R.; Huang, Z.; Wang, K.; Wu, D.; Kang, F.; Zhu, H. Large-area flexible core-shell graphene/porous carbon woven fabric films for fiber supercapacitor electrodes. *Adv. Funct. Mater.* **2013**, *23*, 4862-4869.
21. Yuan, D.; Li, B.; Cheng, J.; Guan, Q.; Wang, Z.; Ni, W.; Li, C.; Liu, H.; Wang, B. Twisted yarns for fiber-shaped supercapacitors based on wetspun PEDOT:PSS fibers from aqueous coagulation. *J. Mater. Chem. A* **2016**, *4*, 11616-11624.
22. Cheng, X.; Zhang, J.; Ren, J.; Liu, N.; Chen, P.; Zhang, Y.; Deng, J.; Wang, Y.; Peng, H. Design of a hierarchical ternary hybrid for a fiber-shaped asymmetric supercapacitor with high volumetric energy density. *J. Phys. Chem. C* **2016,** *120*, 9685-9691.
23. Ramadoss, A.; Kang, K.N.; Ahn, H.J.; Kim, S.I.; Ryu, S.T.; Jang, J.H. Realization of high performance flexible wire supercapacitors based on 3-dimensional $NiCo_2O_4$/Ni fibers. *J. Mater. Chem. A* **2016**, *4*, 4718-4727.
24. Tao, J.; Liu, N.; Ma, W.; Ding, L.; Li, L.; Su, J.; Gao, Y. Solid-state high performance flexible supercapacitors based on polypyrrole-MnO_2-carbon fiber hybrid structure. *Sci. Rep.*, **2013**, *3*, 2286-2292.
25. Ko, T.H.; Radhakrishnan, S.; Seo, M.K.; Khil, M.S.; Kim, H.Y.; Kim, B.S. A green and scalable dry synthesis of $NiCo_2O_4$/graphene nanohybrids for high-performance supercapacitor and enzymeless glucose biosensor applications. *J. Alloys Compd.* **2017**, *696*, 193-200.
26. Dong, X.; Jin, H.; Wang, R.; Zhang, J.; Feng, X.; Yan, C.; Chen, S.; Wang, S.; Wang, J.; Lu, J. High Volumetric Capacitance, Ultralong Life Supercapacitors Enabled by Waxberry-Derived Hierarchical Porous Carbon Materials. *Adv. Energy Mater*. **2018**, *8*, 1702695.
27. Saravanakumar, B.; Jayseelan, S.S.; Seo, M.K.; Kim, H.Y.; Kim, B.S.; $NiCo_2S_4$ nanosheet-decorated 3D, porous Ni film@Ni wire electrode materials for all solid-state asymmetric supercapacitor applications. *Nanoscale* **2017**, *9*, 18819.
28. Kim, N.K.; Kim, W.S.; Jang, H.J.; Chung. Y.S. Fabrication and properties of polyimide-based graphite fibers, *Textile Science and Engineering*, **2020**, *56*, 300-307.
29. Xu, Z.; Sun, S.; Cui, W.; Lv, J.; Geng, Y.; Li, H.; Deng, J. Interconnected network of ultrafine MnO_2 nanowires on carbon cloth with weed-like morphology for high-performance supercapacitor electrodes. *Electrochim. Acta* **2018**, *268*, 340-346.
30. Huang, J.; Chen, L.; Dong, H.; Zeng, Y.; Hu, H.; Zheng, M.; Liu, Y.; Xiao, Y.; Liang, Y. Hierarchical porous carbon with network morphology derived from natural leaf for superior aqueous symmetrical supercapacitors. *Electrochim. Acta* **2017**, *258*, 504-511.
31. Pan, C.; Gu, H.; Dong, L. Synthesis and electrochemcial performance of polyaniline@MnO_2/graphene ternary composites for electrochemical supercapacitors. *J. Power Sources* **2016**, *303*, 175-181.
32. Zhao, Z.; Shen T.; Liu, Z.; Zhong, Q.; Qin, Y. Facile fabrication of binder-free reduced graphene oxide/MnO_2/Ni foam hybrid electrode for high-performance supercapacitors. *J. Alloys Comp*. **2020**, *812*, 152124-152132.
33. Saravanakumar, B.; Ko, T.H.; Kim, B.S. Rational design of binder-free $ZnCo_2O_4$ and Fe_2O_3 decorated porous 3D Ni as high-performance electrodes for asymmetric supercapacitor. *Ceram. Int.* **2018**, *44*, 10635-10645.
34. Wu, M.S.; Chen, F.Y.; Lai, Y.H.; Sie, Y.J. Electrocatalytic oxidation of urea in alkaline solution using nickel/nickel oxide nanoparticles derived from nickel-organic framework. *Electrochim. Acta* **2017**, *258*, 167-174.
35. Ramesh, S.; Yadav, H.M.; Karuppasamy, K.; Vikraman, D.; Kim, H.S.; Kim, J.H.; Kim, H.S. Fabrication of manganese oxide@nitrogen doped graphene oxide/polypyrrole (MnO_2@NGO/PPy) hybrid composite electrodes for energy storage device. *J. Mater. Res. Technol.* **2019**, *8(5)*, 4227-4238.

36. Xiao, A.; Zhou, S.; Zuo, C.; Zhuan, Y.; Ding, X. Controllable synthesis of mesoporous Co_3O_4 nanoflake array and its application for supercapacitor. *Mater. Res. Bull.* **2014**, *60*, 674-678.
37. Sun, X.; Xu, T.; Bai, J.; Li, C. MnO_2 Nanosheets Grown on Multichannel Carbon Nanofibers Containing Amorphous Cobalt Oxide as a Flexible Electrode for Supercapacitors. *ACS Appl. Energy Mater.* **2019**, *2*, 8675-8684.
38. Zhao, J. Li, Z.; Yuan, X.; Yang, Z.; Zhang, M.; Meng, A.; Li, Q. A High-Energy Density Asymmetric Supercapacitor Based on Fe_2O_3 Nanoneedle Arrays and $NiCo_2O_4/Ni(OH)_2$ Hybrid Nanosheet Arrays Grown on SiC Nanowire Networks as Free-Standing Advanced Electrodes. *Adv. Energy Mater.* **2018**, *8*, 1702787.
39. Wang, X.; Liu, Y.; Arandiyan, H.; Yang, H.; Bai, L.; Mujtaba, J.; Wang, Q.; Liu, S.; Sun, H. Uniform Fe_3O_4 microflowers hierarchical structures assembled with porous nanoplates as superior anode materials for lithium-ion batteries. *Appl. Surf. Sci*. **2016**, *389*, 240-246.
40. Oyedotun, K.O.; Masikhwa, T.M.; Mirghni, A.A.; Mutuma, B.K.; Manyala, N. Electrochemical properties of asymmetric supercapacitor based on optimized carbon-based nickel-cobalt-manganese ternary hydroxide and sulphur-doped carbonized iron-polyaniline electrodes. *Electrochim. Acta* **2020**, *334*, 135610.
41. Du, Y.; Li, G.; Chen, M.; Yang, X.; Ye, L.; Liu, X.; Zhao, L. Hollow nickel-cobalt-manganese hydroxide polyhedra via MOF templates for high-performance quasi-solid-state supercapacitor. *Chem. Eng. J.* **2019**, *378*, 122210.
42. Bai, X.; Cao, D.; Zhang, H. Simultaneously morphology and phase controlled synthesis of cobalt manganese hydroxides/reduced graphene oxide for high performance supercapacitor electrodes. *Ceram. Int*. **2020**, *46*, 19135-19145.
43. Guo, Y.; Zhang, S.; Wang, J.; Liu, Z.; Liu, Y. Facile preparation of high-performance cobalt-manganese layered double hydroxide/polypyrrole composite for battery-type asymmetric supercapacitors. *J. Alloys Comp.* ***2020**, 832, 154899-154911.*
44. Nath, A.R.; Jayachandran, A.; Sandhyarani, N. Nanosheets of nickel, cobalt and manganese triple hydroxides/oxyhydroxides as efficient electrode materials for asymmetrical supercapacitors. *Dalton Trans*. **2019**, *48*, 4211-4217.
45. Li, M.; Cheng, J.P.; Wang, J.; Liu, F.; Zhang, X.B. The growth of nickel-manganese and cobalt-manganes layered double hydroxides on reduced graphene oxide for supercapacitor. *Electrochim. Acta* **2016**, *206*, 108-115.
46. Wenping, Y.; Xinyue, S.; Yan, L.; Pang, H. Manganese-doped cobalt zeolitic imidazolate framework with highly enhanced performance for supercapacitor. *J. Energy Storage* **2019**, *26*, 101018-101024.

Sample Availability: Samples of the compounds ...... are available from the authors.